International Journal of Bioprinting

RESEARCH ARTICLE

Fabrication of large-scale scaffolds with microscale features using light sheet stereolithography

Alejandro Madrid-Sánchez*, Fabian Duerr, Yunfeng Nie, Hugo Thienpont, Heidi Ottevaere

Department of Applied Physics and Photonics, Brussels Photonics (B-PHOT), Vrije Universiteit Brussel and Flanders Make, Pleinlaan 2, B-1050 Brussels, Belgium

(This article belongs to the *Special Issue: Novel Materials and Processing for Medical 3D Printing and Bioprinting*)

***Corresponding author:**
Alejandro Madrid-Sánchez
(alejandro.madrid.sanchez@vub.be)

Citation: Madrid-Sánchez A, Duerr F, Nie Y, *et al.*, 2023, Fabrication of large-scale scaffolds with microscale features using light sheet stereolithography. *Int J Bioprint*, 9(2): 650. https://doi.org/10.18063/ijb.v9i2.650

Received: July 29, 2022

Accepted: September 20, 2022

Abstract

The common characteristics that make scaffolds suitable for human tissue substitutes include high porosity, microscale features, and pores interconnectivity. Too often, however, these characteristics are limiting factors for the scalability of different fabrication approaches, particularly in bioprinting techniques, in which either poor resolution, small areas, or slow processes hinder practical use in certain applications. An excellent example is bioengineered scaffolds for wound dressings, in which microscale pores in large surface-to-volume ratio scaffolds must be manufactured – ideally fast, precise, and cheap, and where conventional printing methods do not readily meet both ends. In this work, we propose an alternative vat photopolymerization technique to fabricate centimeter-scale scaffolds without losing resolution. We used laser beam shaping to first modify the profile of the voxels in 3D printing, resulting in a technology we refer to as light sheet stereolithography (LS-SLA). For proof of concept, we developed a system from commercially available off-the-shelf components to demonstrate strut thicknesses up to 12.8 ± 1.8 μm, tunable pore sizes ranging from 36 μm to 150 μm, and scaffold areas up to 21.4 mm × 20.6 mm printed in a short time. Furthermore, the potential to fabricate more complex and three-dimensional scaffolds was demonstrated with a structure composed of six layers, each rotated by 45° with respect to the previous. Besides the demonstrated high resolution and achievable large scaffold sizes, we found that LS-SLA has great potential for scaling-up of applied oriented technology for tissue engineering applications.

Keywords: Scaffolds; Wound dressing; Bioprinting; Stereolithography; Light sheet; Tissue engineering

1. Introduction

Artificial scaffolds have been proposed as pillars to provide structural stability and a suitable environment for bone, organ, and tissue regeneration. Although scaffolds are engineered for very different anatomical structures, they typically have physical and functional properties in common that make them highly relevant for multiple medical applications[1,2]. For instance, scaffolds are highly porous structures as they consist of void spaces within the material. Due to their high porosity, scaffolds exhibit high permeability, which allows blood vessel ingrowth, nutrient diffusion, oxygen transport, and waste removal[2-5]. In addition, the properly selected fabrication materials[6-8], pore size, and distribution promote the adhesion, proliferation, and differentiation of cells[9,10] and influence the mechanical properties of scaffolds for its target applications[4,5,11]. Their structural properties and fabrication technologies are of great research interest in today's tissue engineering.

Bioengineered wound dressing is one of the applications where scaffolds have been widely implemented in research and industry[12-14]. Wound dressings are used to protect the tissue injury site from further mechanical and microbial stress, and maintain proper moisture and temperature at the wound bed[15]. In medical field, the benefits introduced by bioengineered wound dressings have contributed to an accelerated and improved healing process of the injured tissue[8], including optimal management and cost reduction of wound treatments in the health system[16-19]. However, the large surface-to-volume ratio characteristics of wound tissues make the fabrication of engineered scaffolds a complex technological challenge[20-22]. The first reason is the need of large size wound dressings. In daily cases, the wounds, for example, ulcers and burns, can extend from a few millimeters up to a great extension of the human body. Particularly, investigations on burn wound dressings reported a minimum average area of 872 cm^2 of a functionalized wound dressing used in a sample group of 50 patients[23], requiring multiple applications of wound dressing substitute. Furthermore, medical specialists have pointed out the importance of large size wound dressings by quoting that a wound dressing size between 50 × 50 mm^2 to 400 × 400 mm^2 is preferred by medical practitioners[24], suggesting that new fabrication approaches must be developed to reduce the cost of such large bioengineered wound dressings. The second reason lies in the fine struts that provide the scaffold's structure with the properties to closely mimic the native tissue microenvironment. The pores within the scaffold consist of void space within the material, and its physical characteristics, such as size, geometry, or interconnectivity, are determined by choosing the strut position and orientation (in other works, the word "filament"[11] or "fiber"[25] is used to refer to strut, the structuring element of the scaffold). Many studies have shown that the pores in a scaffold not only promote the migration of nutrients, oxygen, and cells but also influence the physical properties of the scaffolds, such as mechanical properties[5], absorption[26], and permeability[3,5]. Thus, in terms of fabrication, the pores in an engineered scaffold require high-resolution capabilities, limiting the scaling-up possibilities of technology. Investigations on the pore size have shown a positive impact on cellular behavior for pore size that ranges from ≈ 20 μm to 150 μm[25,27], from which it was pointed out that an average pore size of 100 μm may work as a promising size[27]. Although the ideas of producing large size items with high precision have not been integrated in the fabrication of bioengineered wound dressing, the achieved progress in tissue engineering allows for targeting specific scaffold's designs and fabrication strategies to pave the way on the fabrication of this type of scaffolds as requested by medical specialists.

Many available commercial bioengineered wound dressings result from technologies such as freeze-dry[28] and electrospinning[29]. Both technologies allow for centimeter-scale scaffold fabrication with highly porous characteristics. However, these technologies are constrained in their ability to control the pore size and distribution, leading to limited pore distributions with large size deviations[25] (40 – 150 μm in the same fabrication process) and low pore interconnectivity (tubular or superficial)[25,26,29,30]. The latter is recognized as the key feature for the permeability and migration properties of the scaffolds.

On the other hand, three-dimensional (3D) bioprinting has emerged as a fabrication technique, which is highly accepted, in the field of tissue engineering due to its free-form 3D fabrication framework, high resolution, and variety of biocompatible materials. Bioprinting allows for complex pore patterning, high repeatability, and interconnectivity in engineered scaffolds[9,31-33]. At present, extrusion[34]- and jetting[35]-based bioprinting play a major role in tissue substitute fabrication because of their capabilities to construct cell-laden scaffolds and control cell density, location, and model geometries. Among 3D bioprinting methods, both material extrusion and material jetting methods possess the most versatile and low-cost configurations to construct cell-laden scaffolds of multiple cells and soft materials (bioinks), making these technologies attractive options to researchers[34,35]. Nevertheless, inability to fabricate sub-micron structures, their dependence on nozzles, and mechanical translational stages hinder bioprinting techniques in rapid fabricating of large size substitutes with fine structures that mimic the native tissue microenvironment.

Among the 3D bioprinting technologies, vat photopolymerization (VP)-based bioprinting is currently the only technique that can fabricate with the highest resolution and precision[36,37]. VP techniques use light radiation to harden a liquid material locally using polymerization. By steering a laser beam or projecting a two-dimensional (2D) image on the liquid material, a 3D object is realized in a layer-by-layer approach. One of the most widely used technologies in 3D scaffold fabrication is direct light processing (DLP)[37-40]. Its ability to expose a photosensitive material to a full 2D image projection has resulted in 3D structures with ultra-high resolution as well as size and printing speed not possible to fabricate using counterpart methods, such as stereolithography (SLA) and two-photon polymerization (TPP)[37]. For example, investigations on the optimization of the projection optics of DLP devices led to 3D constructions with a lateral resolution of 4.1 µm and an axial resolution of 2.5 µm in acrylate-based resins against 75 µm resolution in SLA[41]. In addition, at the highest resolution, the projection area achieved with DLP was 6.4 × 4 mm², against the tens of micrometers typically found in TPP processes[41,42]. Losing some tens of microns in resolution to gain larger area expositions have directed many DLP devices into the fabrication of 3D constructs with lateral resolution that ranges between 20 and 100 µm, achieving, for example, a maximum projection area of 19.35 × 12.1 mm² at the maximum lateral resolution[43]. The results achieved by DLP set a benchmark in 3D bioprinting technologies and pave the way toward rapid and high-precision manufacturing.

However, the magnification or resolution dependence of DLP due to the projection optics and digital micromirror devices (DMDs) hinder the scaling-up capabilities of rapid and high-resolution 3D printing (e.g., down to several millimeters in size)[38,39,44-46], making its implementation impractical in large surface-to-volume ratio constructs found in wound dressing applications[30,46-48]. Furthermore, although stitching methods have been proposed to fabricate larger areas in state-of-the-art, the printed structures exhibit inaccuracies, surface defects, and mechanical deformations that may affect the performance of the scaffolds[38,47,49]. It is worth mentioning that more research must be carried out on the stitching effects of biomaterials on scaffold fabrication.

The requirement of scaffolds exhibiting large surface-to-volume ratios can only be satisfied with novel manufacturing strategies that comprise different exposure, fabrication, and structuring modes. In this paper, we propose an alternative technique that extends the capabilities of VP devices toward practical large size scaffold fabrication with microscale features. Instead of using the common projection systems found in DLP and based on the laser scanning setup of SLA devices, we use laser beam shaping to modify the profile of the voxels in 3D printing, resulting in a technology we call light sheet SLA (LS-SLA). We showed that it is possible to produce elongated voxels to conserve an excellent lateral resolution for a large printing area, resulting in submicron resolution for centimeter length exposures without stitching structures. Furthermore, the fact that the performance of the system now depends on laser beam characteristics instead of used projection devices opens up the possibility for further improvement in the aspects of scaffold fabrication of even larger sizes and shorter fabrication times as we demonstrated in this work.

2. Methods and printing protocol

2.1. LS-SLA

The 3D printer developed in this work is based on a VP bottom-up fabrication scheme (Figure 1A)[41]. The polymer resin is in contact with the bottom surface (FEP film) of the resin vat and an inverted build platform, which is used to control the height of the resin layer. The pattern on each layer is built by the selective light exposure of the polymer resin to a blue laser light (405 nm) that is focused on the bottom surface of the resin vat. Thereby, the exposed regions are hardened through polymerization of the resin, which subsequently adheres to the build platform. The elemental hardened structures are referred to as struts and voxels in this work. After polymerization of one layer sequence, the build platform moves stepwise in the z-direction, allowing new liquid resin to flow into the bottom of the resin vat before the process repeats.

In this work, we propose breaking the symmetry of the illumination source of conventional VP systems by producing large length-to-width aspect ratio voxels. The elongated voxels are created using cylindrical lenses. Due to its curved face in only one plane of symmetry, the laser beam propagates in the same path with two possible configurations[50]. In one configuration, as depicted in the top diagram of Figure 1B, the light propagating from a beam shaper passes through the cylindrical lens without any effect. Then, the laser beam is focused on one of the axes of the film plane producing a LS with a width only limited by diffraction at the scan lens aperture. The achievable width of the LS at the film plane is estimated using Equation 1.

$$d=\kappa\lambda(F/\#) \tag{1}$$

Where, $F/\#$ is the F-number of the scan lens, λ is the wavelength of the light source, and k is a truncation factor with a value $\kappa = 2.44$ for a uniform illuminated entrance pupil of the scan lens[51].

The second dimension controls the length of the LS. In the bottom configuration of Figure 1B, the curvature of the cylindrical lens in combination with the scan lens forms a collimated beam expander and magnifies the height of the rectangle beam delivered by the beam shaper. The magnification of the Y-Z configuration is determined by the ratio between the effective focal lengths f_{sl} of the scan lens and the cylindrical lens f_{cl}, as shown in Equation 2.

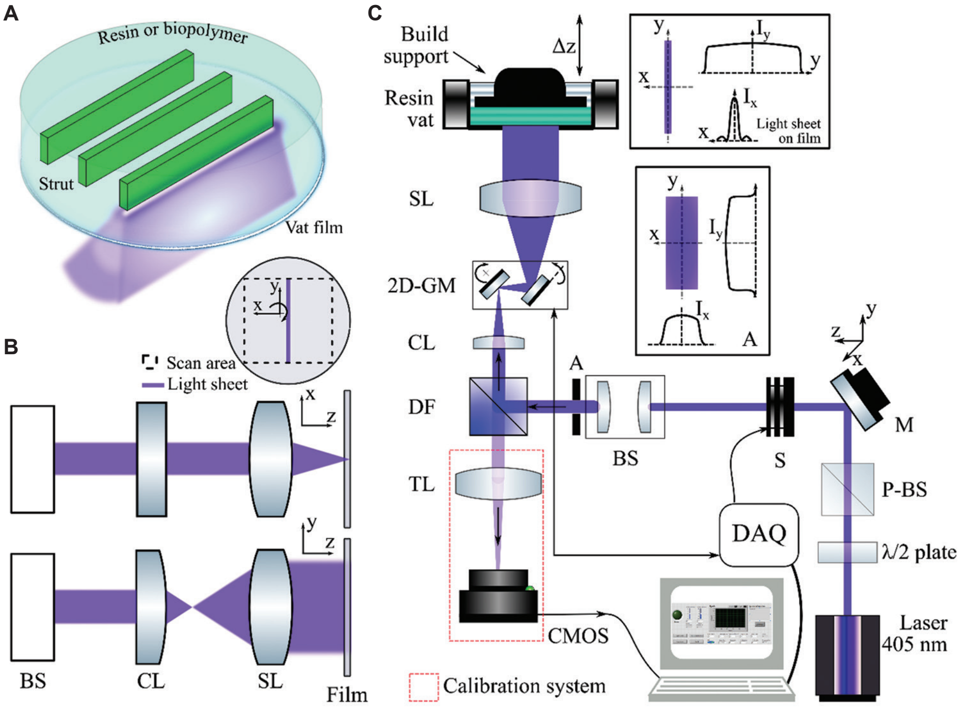

Figure 1. (A) Local illumination of a light sheet in a bottom-up 3D printer configuration. (B) Generation of light sheet-based optical system with two planes of symmetry. (C) Schematic of the built light sheet SLA device. M: Mirror; S: Mechanical shutter; BS: Beam shaper; DF: Dichroic filter; CL: Cylindrical lens; GM: Galvano mirror scanner; SL: Scan lens; TL: Tube lens; LS-LSA: Light sheet stereolithography.

$$M_{YZ}=f_{sl}/f_{cl} \tag{2}$$

In the first approximation, Equations 1 and 2 help to determine the proper characteristics of the lenses needed in the system. In addition, the scan lens combined with a mechanical Galvano mirror scanner steers the LS in different positions of the film plane.

2.2. Demonstrator device

We proved our concept with commercially available components. Only few mechanical elements, such as the resin vat and the build support, were customized in our facilities. A complete schematic of the designed and implemented system is shown in Figure 1C. First, the laser source (405 nm) is propagated through a power attenuator system (λ/2-plate and polarized beam-splitter, P-BS) to control the radiant exposure of the printing process. The laser beam is then propagated through a beam expander and an irradiance distribution conditioner, the beam shaper. The latter consists of two cylindrical lenses with effective focal length EFL = 25 mm and EFL = 125 mm. In combination with the rectangular aperture A (4 × 20 mm^2 at plane A, Figure 1C), the beam shaper converts the Gaussian distribution of the laser beam into a uniform irradiance with a rectangular boundary, which is used to produce the LS with uniform illumination at the FEP film (resin vat plane, Figure 1C). The LS illumination is achieved by combining one cylindrical lens (EFL = 50 mm) and the telecentric scan lens (CLS-SL, Thorlabs Inc., United States). The two-plane symmetry introduced by the cylindrical lens elongates the beam in one orientation (y-axis) and focuses the beam in the other one (x-axis), which results in LSs with large length-to-width aspect ratios (l/w~1100). To produce the patterns on the bottom surface of the resin vat along the complete field of view (FOV) of the scan lens, two Galvano mirrors (GVS202, Thorlabs Inc.) were positioned near the front focal point of the scan lens. The rotational angles of the Galvano mirrors expose the resin at different positions along the resin plane with an exposure time controlled by the mechanical shutter (beam shutter). All the opto-electro-mechanical components were controlled by an application we developed in the software LabView, which is interfaced with a data acquisition device (National Instruments, United States).

2.2.1. Alignment system

The alignment of the LS on the bottom surface of the resin vat takes place before starting the structuring sequence. The alignment is performed by collecting the reflected light from the FEP film with the scan lens and focusing the light back on a CMOS sensor, as shown in the calibration system of Figure 1C. The LS produced on the sensor is a magnified image of the LS used to illuminate the resin vat.

The alignment system consists of the scan lens (CLS-SL, Thorlabs Inc.), the cylindrical lens located before the scan lens, the tube lens TL (TTL200-A, Thorlabs Inc.), and the CMOS camera (Mako U-130, Allied Vision).

2.2.2. Patterns generated with LS illumination

Patterns were generated by scanning and changing the angular orientation of the LS with respect to the building platform. As mentioned earlier, scanning was performed in our system using a Galvano mirror that steers the LS along the FOV of the scan lens. This allows for printing structures along one direction and controlling the steps between successive linear voxels with high precision. A pattern can consist of linear voxels with different orientations, as can be found in a rectangular scaffold; therefore, changing the orientation of the LS becomes important. In our system, we modified the orientation of the LS by rotating the building platform or rotating the beam shaping optics. The scaffolds presented in this work were printed following the first strategy.

2.3. Scaffold fabrication

Many features of a scaffold geometry can be controlled by the position and orientation of the strut, including pore size, pore shape, pore volume fraction, and as demonstrated in other works, mechanical properties and functional gradients of the scaffold[11]. In this work, we used two patterns to demonstrate the capabilities of LS illumination in controlling these features. The first scaffold comprises 0/90° struts composed of a set of uniform and rectangular pores, as shown in Figure 2A. To fabricate such a scaffold with 3D LS printing, 0° struts were distributed periodically along the FOV of the scan lens with controlled spacing. Then, the LS orientation was rotated 90° with respect to the previous pattern and the second pattern was printed at the same layer. Subsequently, a set of layers of the same 0/90 pattern might be printed on top of one another to build a 3D scaffold. Other types of pore shapes and interconnectivity were achieved by changing the orientation of the struts.

Figure 2B shows a scaffold with 0/45/90 orientation. In this configuration, we opted for printing each orientation pattern at a different layer, which leads to higher porosity ratios and more complex pore interconnectivity. While the control of the pore size, shape, distribution, and strut resolution are demonstrated in this paper with the two scaffold configurations in Figure 2, the capabilities of the 3D LS printer can be extended to more complex patterns following the same principles of scanning and rotating the LS.

2.4. Resin material

We demonstrated the proof of concept of our prototype with the commercial low-shrinkage Elegoo resin (Elegoo, Shenzhen, China), which allowed us to assess the performance of the novel LS printer in terms of speed, scale, and resolution. The material used in this work is a one-photon polymerization resin used in conventional and commercial SLA-DLP systems to fabricate pieces with strong mechanical properties. As in any one absorption polymerization material, the curing height (C_p) and transversal resolution in a 3D-printed structure can be described in terms of radiant exposure (E) as predicted by the Beer-Lambert law[52]. Those characteristics are estimated by the working curve of the resin, Equation 3, which we obtained by measuring the height of various polymerized solids printed under different exposure conditions. We found that the resin exhibits a penetration depth of D_p = 110.95 µm and a critical exposure of $E_c = 1.9\ mJ/cm^2$.

$$C_p = D_p \ln (E/E_c) \tag{3}$$

2.5. Printing protocol

The printing protocol we used during the experiments is highlighted in Figure 2C. First, the LS was aligned and the start position of the build platform was set with respect to the FEP film of the resin vat. Then, the radiant exposure E and exposure time t (typically < 0.1 s) are defined accordingly to the desired curing depth C_p, e.g., ≈150 µm, for which the irradiance I at the FEP film is adjusted properly with the expression $E = I_t$. These printing conditions combined with the geometrical parameters of the scaffold, for example, the number of struts and pore size, constitute the set of values we introduced in our custom-build application developed in LabView (National Instruments). At this stage, we filled the resin vat with 5 mL of resin to guarantee the immersion of the build surface. In general, resins exhibit good adhesion to metallic surfaces, but they can vary between formulation and materials, specifically when working with biopolymers. While working with high porous and thin layers, we found aluminum plates and glass substrates good adherent materials for the polymerized structures. These types of materials also guarantee the fabrication of complete 3D scaffolds. However, fixation of fine structures is largely improved when functionalizing the glass substrates with 3-(Trimethoxysilyl)propyl methacrylate. We followed the procedure described in Sigma-Aldrich[53] to attach the scaffolds to the glass substrates during the printing process. After printing, the scaffold was rinsed and kept in isopropanol 99%.

2.6. Scaffold measurement and characterization

We characterized the scaffolds with respect to the strut and pore size, the pore distribution, the overall size, and the pore interconnectivity. To obtain a complete physical characterization of the scaffolds, we used a Keyence digital microscope with ×200 (Keyence, Japan). The illumination

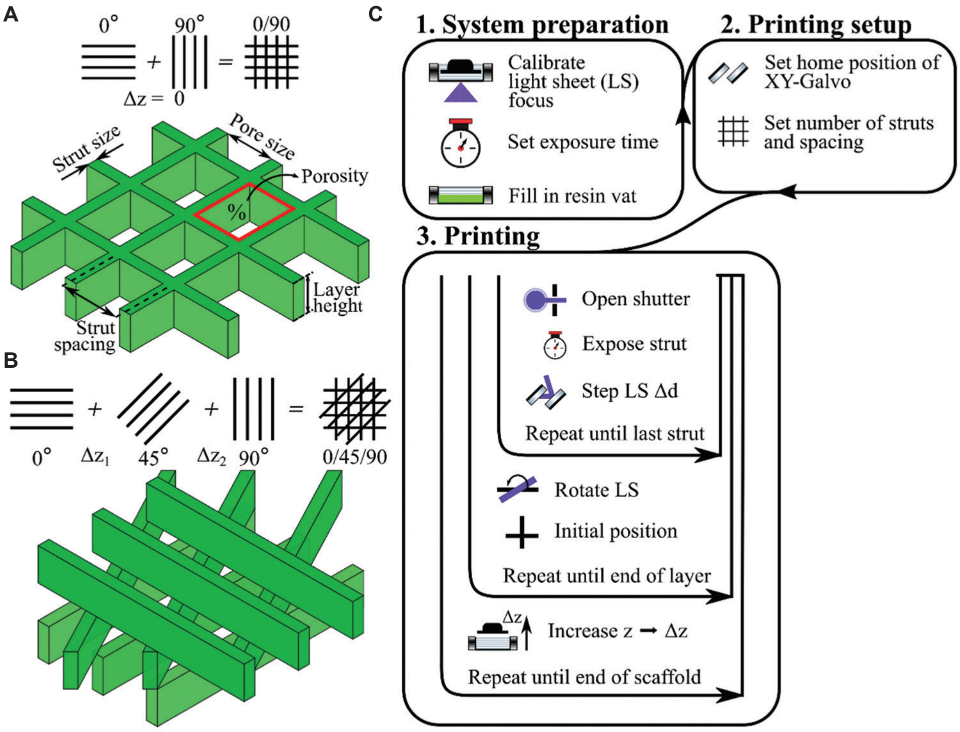

Figure 2. (A) Fabrication pattern of a 0/90 scaffold. (B) Fabrication pattern of a 3D 0/45/90 scaffold. (C) Flowchart of LS-SLA printing. LS-LSA: Light sheet stereolithography.

setup comprised a transmitted brightfield in combination with reflected LED illumination, which accurately measured the struts and pores of the scaffold. Complete images of the scaffolds were acquired while retaining the microscale characteristics. We stitched a sequence of 2D images in combination with 3D depth composition for focused and height correction.

The porosity of the scaffolds was further analyzed with fluorescence microscopy. Therefore, we used fluorescent microspheres (Cospheric LLC, United States) with sizes ranging between 63 and 75 µm and immersed into the scaffold with a phosphate-buffered saline (PBS). Fluorescence images were obtained with a Leica SP8X inverted confocal fluorescence microscope (Leica Microsystems, Germany) using laser illumination (405 nm and 575 nm) and a 10X/NA0.4 microscope objective. 3D scaffolds were measured with a laser confocal microscope (OLS5000, Olympus, Japan) using a ×20 microscope objective. The z-layer scanning was performed with a height step of 1.2 µm and a scanning area that covers 647 × 647 µm^2.

3. Results and discussion

3.1. Strut, pore, and scaffold sizes

In VP, the strut or voxel size and position determine the characteristics of the pores and extension within a scaffold. Particularly, DLP method has demonstrated micron features fabrication in scaffolds; however, due to its dependence on projection systems, the resolution in this type of systems is compromised (≥50 µm) when large surface structures are needed[39,54,55]. As mentioned before, LS-SLA provides an alternative fabrication technology for highly porous scaffolds with large surface-to-volume ratio due to its ability to construct large length-to-width ratio struts. To demonstrate the ability of LS-SLA to fabricate high-resolution struts and small pores while delivering centimeter scale scaffolds, we printed scaffolds in three printing conditions, which are summarized in the experimental results shown in Figure 3. Three rectangular scaffolds consisting of 500 struts with 0/90 orientation, constant strut spacing and a layer height of 100 µm were fabricated at radiant exposure values of 12.6 mJ/cm^2, 16.9 mJ/cm^2, and 33.7 mJ/cm^2.

The exposure was adjusted by keeping the irradiance at the FEP film constant and using exposure times of 0.03 s, 0.04 s, and 0.08 s, respectively. The results of the chosen printing conditions are shown in Figure 3A-C, respectively. Figure 3A shows the strut and pores distribution at the lowest chosen exposure. At an exposure of 12.6 mJ/cm^2, we demonstrated a strut size of 12.8 ± 1.8 µm standard deviation (n = 6) with a pore size of 71.7 ± 3.2 µm. The latter is the biggest pore size within the three chosen

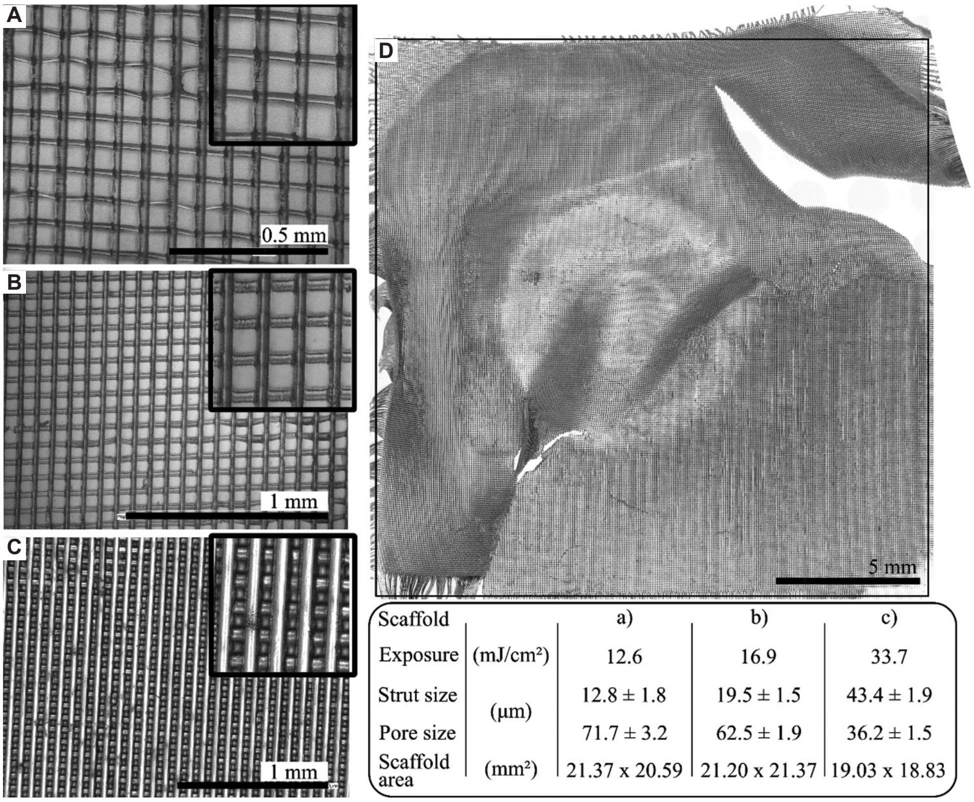

Scaffold		a)	b)	c)
Exposure	(mJ/cm²)	12.6	16.9	33.7
Strut size	(μm)	12.8 ± 1.8	19.5 ± 1.5	43.4 ± 1.9
Pore size		71.7 ± 3.2	62.5 ± 1.9	36.2 ± 1.5
Scaffold area	(mm²)	21.37 x 20.59	21.20 x 21.37	19.03 x 18.83

Figure 3. (A-C) Microscope images of the built scaffolds at three different exposure values show the size and distribution of strut and pore. The square shows a zoom-in region from the same pictures. (D) Overall view of the complete scaffold shown in (C). Fractures are generated during manipulation.

printing conditions. Exposure, exposure time, and laser power define the printing conditions that can be tuned in our system to modify the strut size and the printing time of the scaffold. Balancing those parameters can significantly reduce the printing time and deliver the greatest throughput in terms of resolution and precision. For example, the strut size of the scaffolds shown in Figure 3B and C was increased up to 43.4 ± 1.9 µm (*n* = 6), inducing the reduction of the pore size down to 36.2±1.5 µm at a constant strut spacing. Furthermore, structures built with LS-SLA depict large surface fabrication. Two-D stitched images of the scaffolds shown in Figure 3 demonstrate that LS-SLA can build structures of large area and simultaneously conserves microscale struts (<50 µm). Figure 3D shows a 2D stitched image of the scaffold shown in Figure 3C with a measured area of 19.09 mm × 18.83 mm. At the smallest strut size, 12.8 µm, the strut length-to-width ratio was $l/w = 1696$ for a scaffold with an area of 21.37 × 20.59 mm^2.

3.2. Pore size control and uniformity

In practical terms, it is easier to fix the exposure conditions with respect to the desired resolution and steer the LS along the scanning area. Steering the LS allows illuminating at different positions and consequently controlling the pore size within the scaffold. It has been demonstrated that the scaffold can be functionalized for different cell types. Furthermore, specific properties can be improved by modifying the size distribution of the pores within the scaffold[27]. Furthermore, the precision of the available scanning systems has greatly increased, which benefits scaffold fabrication in pore size control and uniformity. To illustrate, we fabricated two scaffolds of different strut spacing. Figure 4A shows the fluorescence image of a scaffold with a pore size of 68 ± 2.5 µm (*n* = 11), and Figure 4B shows the scaffold that exhibits a pore size of 149.9 ± 2.3 µm (*n* = 10). Microspheres (diameter ranging from 63 µm to 75 µm) were pipetted with PBS within both scaffolds and imaged with fluorescence microscopy as depicted by the red circles in Figure 4. The microspheres stress the porous characteristics of the scaffolds fabricated with LS-µ-SL. On one side, the microspheres were filtered out or kept in suspension by the small pores of the scaffold (Figure 4A). On the other side, the microspheres flowed within the pores of the scaffold since the pore size was ≈ 2 times larger than the diameter of the microspheres in (Figure 4B). In general, the results presented in Figure 4 mimic the property of permeability in highly porous scaffolds.

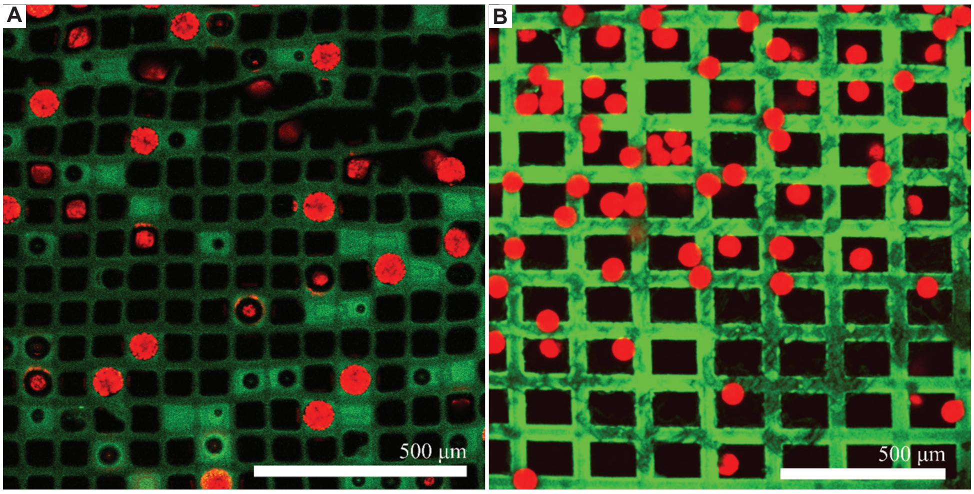

Figure 4. Fluorescence images of microsphere pipetted inside the scaffold with a pore size of (A) 68 ± 2.5 µm and (B) 149.9 ± 2.3 µm.

3.3. Three-dimensional interconnectivity

Finally, we demonstrated the 3D printing of scaffolds using our prototype device. Figure 5A shows a top view of the microscopic structure of the 3D scaffold fabricated in this work. The scaffold consists of a series of six layers with 45° orientation within each other. Each layer consists of 100 struts that took a printing time of 3.5 s/layer. The scaffold has orientations 0/45/90/135/180° with one additional layer as a base. Each layer height was set by the building support with a value of 100 µm. Figure 5B shows a 3D reconstruction from confocal microscopy imaging, which evidences the different height values of the layers within the construct and demonstrates the void spaces created along the surface and between each layer. A height range of ≈ 526 µm was reconstructed in Figure 5B. Figure 5C shows a computer-assisted design model of a small section of the fabricated scaffold, and the 3D pore is represented by the blue volume contained within the struts. An internal section of the 3D pore model evidences high interconnectivity within the pores due to 3D fabrication, which may influence efficiency of cell ingrowth[5], migration[25], and directionality[45]. In addition, engineered 3D pores promote water penetration, as well as influence the transmission of vapors and the diffusion of nutrients and waste[8].

3.4. Prospects

It is hard to imagine that one technology could overcome all fabrication-related challenges in tissue engineering. The resolution and printing area in 3D bioprinting technologies remain a huge challenge that needs to be addressed. In addition, hybrid and customized approaches can provide a solution to large-scale fabrication. LS-SLA is developed to support this purpose. Alternatively, we propose looking at other illumination shapes to support VP-based bioprinting with a technology that provides high resolution without sacrificing printing areas. Although its linear voxel shape may constrain free-form fabrication, many studies have demonstrated the benefits of highly porous scaffolds based on linear struts to cell regeneration[9,13,45]. Some examples are the mesh-like structures used in commercial wound dressings[13] and other fibrous bioengineered scaffolds fabricated with sophisticated methods[25]. However, in DLP technology, the resolution and projection area are limited by the magnification of the optics and the current DMD[56]. To the best of our knowledge, the maximum area printed at a lateral resolution similar to the size achieved in this work is 19.35 mm × 12.1 mm[41]. The projection area in that case corresponds to the limit of DMD technology for near ultraviolet sources[57]. In contrast, due to the independence from projection systems in LS-SLA, the line length of the struts can be enlarged while conserving its width. Beyond the large strut length and width aspect ratio demonstrated in this work, both dimensions can be further optimized by the optical characteristics of the scan lens as initially estimated with Equations 1 and 2[58,59]. Available commercial scan lenses with larger FOVs and resolution as the one selected in this work support the idea that the validated concept allows for improvement and scaling-up opportunities for bioprinting technologies used in tissue engineering[60,61]. Finally, application-oriented solutions as demonstrated with LS illumination may positively boost the health industry and research on the fabrication of larger scaffolds with high pore control and resolution. With an increasing research interest on new biomaterials for VP[32,62], its techniques may rapidly join in as a key technology in the research and industry of tissue engineering.

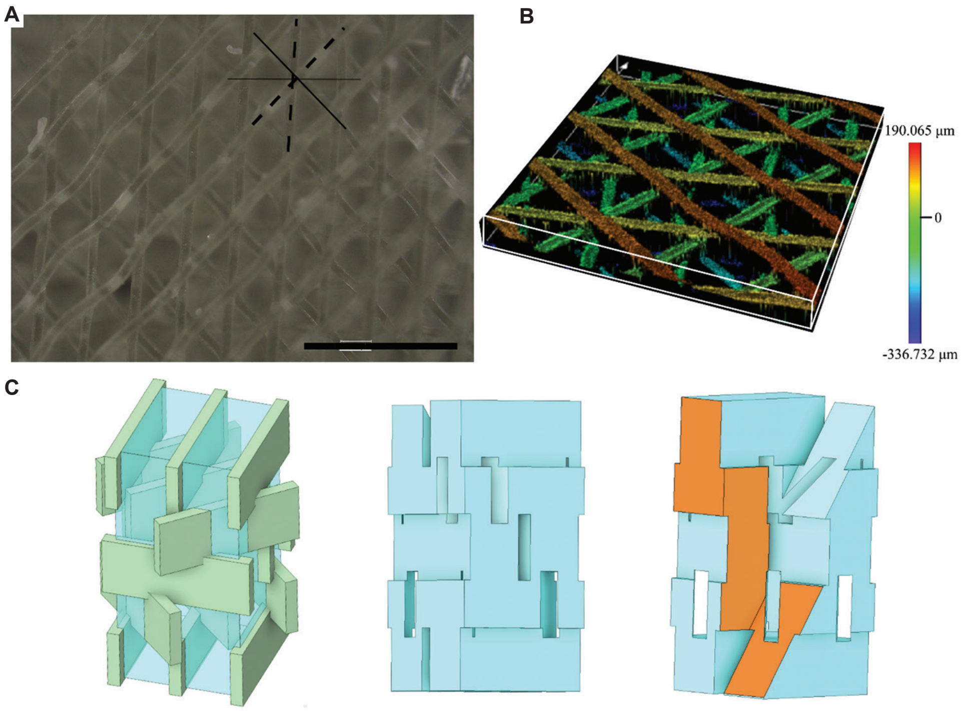

Figure 5. (A) Microscope image taken from the top of the six layers scaffold. The black lines depict the pattern orientations (scale bar: 500 µm). (B) 3D reconstruction of a segment from the same scaffold performed using confocal microscopy. The colors in the struts and the color bar show the height of the top of the layers. (C) Computer-assisted design model of the pore morphology in a 3D construct represented by the blue volume contained within the struts.

4. Conclusions

This work presents a 3D scaffold printing approach by implementing LS illumination on conventional VP. We built a proof-of-concept demonstrator using commercial components and demonstrated its ability to fabricate scaffolds with microscale features using linear voxels as structuring element. The results show printed scaffolds with high resolution: A strut thickness of 12.8 ± 1.8 µm, tunable and uniform pore sizes ranging from 36 µm to 150 µm, and a large size fabrication with areas up to 21.4 mm × 20.6 mm. Based on the results shown in this work, we demonstrated that LS printing is able to provide a large printing area while conserving the fabrication of small features in one direction with length-to-width ratios that can easily surpass a value of $l/w = 1600$. Therefore, large structures (>400 mm^2) with micrometer features (<20 µm) can be fabricated at high speeds (>700 mm/s) and short printing times (<3.5 s/layer). Furthermore, the ability to construct complex and 3D architectures was demonstrated with a scaffold composed of six layers of 45°-oriented patterns, which can benefit the fabrication of architectures that regulate cell ingrowth, oxygen, and nutrient diffusion with tailored mechanical properties. Finally, our promising results on the commercially available components clearly highlight the prospects for scaling-up and enhancing this approach for tissue engineering applications.

Acknowledgments

The authors wish to acknowledge the assistance given by Julie Verdood and Tatevik Chalyan in performing the image acquisition of the samples using the measurement equipment available at Brussels Photonics, Vrije Universiteit Brussel.

Funding

This study was financially supported by Fonds Wetenschappelijk Onderzoek (G044516N and 1252722N), Vrije Universiteit Brussel (Hercules, Methusalem, OZR), and H2020 Future and Emerging Technologies (FET-OPEN No.829104, SensApp).

Conflict of interest

The authors declare no conflicts of interest.

Author contributions

Conceptualization: Alejandro Madrid Sánchez, Fabian Duerr, Yunfeng Nie, and Heidi Ottevaere
Funding acquisition: Heidi Ottevaere
Investigation: Alejandro Madrid Sánchez
Resources: Hugo Thienpont and Heidi Ottevaere
Validation: Alejandro Madrid Sánchez
Writing – original draft: Alejandro Madrid Sánchez

Writing – review & editing: Alejandro Madrid-Sánchez, Fabian Duerr, Yunfeng Nie, Hugo Thienpont, and Heidi Ottevaere

Ethics approval and consent to participate

Not applicable.

Consent for publication

Not applicable.

Availability of data

Not applicable.

References

1. O'Brien FJ, 2011, Biomaterials a amp; scaffolds for tissue engineering. *Mater Today*, 14: 88–95.

   https://doi.org/10.1016/S1369-7021(11)70058-X

2. Loh QL, Choong C, 2013, Three-dimensional scaffolds for tissue engineering applications: Role of porosity and pore size. *Tissue Eng Part B Rev*, 19: 485–502.

   https://doi.org/10.1089/ten.teb.2012.0437

3. O'Brien FJ, Harley BA, Waller MA, *et al*., 2006, The effect of pore size on permeability and cell attachment in collagen scaffolds for tissue engineering. *Technol Heal Care*, 15: 3–17.

   https://doi.org/10.3233/THC-2007-15102

4. Perez RA, Mestres G, 2016, Role of pore size and morphology in musculo-skeletal tissue regeneration. *Mater Sci Eng C Mater Biol Appl*, 61: 922–939.

   https://doi.org/10.1016/j.msec.2015.12.087

5. Sobral JM, Caridade SG, Sousa RA, *et al*., 2011, Three-dimensional plotted scaffolds with controlled pore size gradients: Effect of scaffold geometry on mechanical performance and cell seeding efficiency. *Acta Biomater*, 7: 1009–1018.

   https://doi.org/10.1016/j.actbio.2010.11.003

6. Sheikholeslam M, Wright ME, Jeschke MG, *et al*., 2018, Biomaterials for skin substitutes. *Adv Healthc Mater*, 7: 1700897.

   https://doi.org/10.1002/adhm.201700897

7. Phelps EA, García AJ, 2010, Engineering more than a cell: Vascularization strategies in tissue engineering. *Curr Opin Biotechnol*, 21: 704–709.

   https://doi.org/10.1016/j.copbio.2010.06.005

8. Negut I, Dorcioman G, Grumezescu V, 2020, Scaffolds for wound healing applications. *Polymers* (*Basel*), 12: 1–19.

   https://doi.org/10.3390/polym12092010

9. Gauvin R, Chen YC, Lee JW, *et al*., 2012, Khademhosseini, Microfabrication of complex porous tissue engineering scaffolds using 3D projection stereolithography. *Biomaterials*, 33: 3824–3834.

   https://doi.org/10.1016/j.biomaterials.2012.01.048

10. Park S, Kim G, Jeon YC, *et al*., 2009, 3D polycaprolactone scaffolds with controlled pore structure using a rapid prototyping system. *J Mater Sci Mater Med*, 20: 229–234.

    https://doi.org/10.1007/s10856-008-3573-4

11. Gleadall A, Visscher D, Yang J, *et al*., 2018, Review of additive manufactured tissue engineering scaffolds: Relationship between geometry and performance. *Burn Trauma*, 6: 1–16.

    https://doi.org/10.1186/s41038-018-0121-4

12. Yannas IV, Lee E, Orgill DP, *et al*., 1989, Synthesis and characterization of a model extracellular matrix that induces partial regeneration of adult mammalian skin. *Proc Natl Acad Sci U S A*, 86: 933–937.

    https://doi.org/10.1073/pnas.86.3.933

13. Zhong SP, Zhang YZ, Lim CT, 2010, Tissue scaffolds for skin wound healing and dermal reconstruction. WIREs Nanomed Nanobiotechnol, 2: 510–525.

    https://doi.org/10.1002/wnan.100

14. Kus KJ, Ruiz ES, 2020, Wound dressings–a practical review. *Curr Dermatol Rep*, 9: 298–308.

    https://doi.org/10.1007/s13671-020-00319-w

15. Dabiri G, Damstetter E, Phillips T, 2016, Choosing a wound dressing based on common wound characteristics. *Adv Wound Care*, 5: 32–41.

    https://doi.org/10.1089/wound.2014.0586

16. Lindholm C, Searle R, 2016, Wound management for the 21st century: Combining effectiveness and efficiency. *Int Wound J*, 13: 5–15.

    https://doi.org/10.1111/iwj.12623

17. Kröger K, Jöster M, 2018, Prevalence of chronic wounds in different modalities of care in Germany. *EWMA J*, 19: 45–49.

18. Sen CK, 2021, Human wound and its burden: Updated 2020 compendium of estimates. *Adv Wound Care*, 10: 281–292.

    https://doi.org/10.1089/wound.2021.0026

19. Posnett J, Gottrup F, Lundgren H, et al., 2009, The resource impact of wounds on health-care providers in Europe. J Wound Care, 18: 154–154.

    https://doi.org/10.12968/jowc.2009.18.4.41607

20. Powers JG, Higham C, Broussard K, *et al*., 2016, Wound healing and treating wounds. *J Am Acad Dermatol*, 74: 607–625.

    https://doi.org/10.1016/j.jaad.2015.08.070

21. Nichols E, 2015, Wound assessment Part 1: How to measure a wound. *Wound Essent*, 10: 51–55.

22. Lucas Y, Niri R, Treuillet S, *et al*., 2021, Castaneda, Wound size imaging: Ready for smart assessment and monitoring.

Adv Wound Care, 10: 641–661.

https://doi.org/10.1089/wound.2018.0937

23. Verbelen J, Hoeksema H, Heyneman A, *et al.*, 2014, Aquacel® Ag dressing versus Acticoat™ dressing in partial thickness burns: A prospective, randomized, controlled study in 100 patients. Part 1: Burn wound healing. *Burns*, 40: 416–427.

https://doi.org/10.1016/j.burns.2013.07.008

24. Selig HF, Lumenta DB, Giretzlehner M, *et al.*, 2012, The properties of an "ideal" burn wound dressing what do we need in daily clinical practice? Results of a worldwide online survey among burn care specialists. *Burns*, 38: 960–966.

https://doi.org/10.1016/j.burns.2012.04.007

25. Yu H, Chen X, Cai J, *et al.*, 2019, Novel porous three-dimensional nanofibrous scaffolds for accelerating wound healing. *Chem Eng J*, 369: 253–262.

https://doi.org/10.1016/j.cej.2019.03.091

26. Shyna S, Shanti Krishna A, Nair PD, *et al.*, 2020, A nonadherent chitosan-polyvinyl alcohol absorbent wound dressing prepared via controlled freeze-dry technology. *Int J Biol Macromol*, 150: 129–140.

https://doi.org/10.1016/j.ijbiomac.2020.01.292

27. Boekema B.K.H., Vlig M, Olde Damink L, *et al.*, 2014, Ulrich, effect of pore size and cross-linking of a novel collagen-elastin dermal substitute on wound healing. *J Mater Sci Mater Med*, 25: 423–433.

https://doi.org/10.1007/s10856-013-5075-2

28. Ng S, 2020, Freeze-dried wafers for wound healing. In: Ther. Dressings Wound Health. Cupertino, Hoboken: Apple, Wiley, pp137–155.

https://doi.org/10.1002/9781119433316.ch7

29. Dias JR, Granja PL, Bártolo PJ, 2016, Advances in electrospun skin substitutes. *Prog Mater Sci*, 84: 314–334.

https://doi.org/10.1016/j.pmatsci.2016.09.006

30. Cui T, Yu J, Li Q, *et al.*, 2020, Large-scale fabrication of robust artificial skins from a biodegradable sealant-loaded nanofiber scaffold to skin tissue via microfluidic blow-spinning. *Adv Mater*, 32: 2000982.

https://doi.org/10.1002/adma.202000982

31. Pereira RF, Barrias CC, Granja PL, *et al.*, 2013, Advanced biofabrication strategies for skin regeneration and repair. *Nanomedicine*, 8: 603–621.

https://doi.org/10.2217/nnm.13.50

32. Chartrain NA, Williams CB, Whittington AR, 2018, A review on fabricating tissue scaffolds using vat photopolymerization. *Acta Biomate*, 74: 90–111.

https://doi.org/10.1016/j.actbio.2018.05.010

33. Mostafavi A, Samandari M, Karvar M, *et al.*, 2021, Colloidal multiscale porous adhesive (bio)inks facilitate scaffold integration. *Appl Phys Rev*, 8: 041415.

https://doi.org/10.1063/5.0062823

34. Jiang T, Munguia-Lopez JG, Flores-Torres S, *et al.*, 2019, Extrusion bioprinting of soft materials: An emerging technique for biological model fabrication *Appl Phys Rev*, 6: 011310.

https://doi.org/10.1063/1.5059393

35. Li X, Liu B, Pei B, *et al.*, 2020, Inkjet Bioprinting of biomaterials. *Chem Rev*, 120: 10793–10833.

https://doi.org/10.1021/acs.chemrev.0c00008

36. Ng WL, Lee JM, Zhou M, *et al.*, 2020, Vat polymerization-based bioprinting—process, materials, applications and regulatory challenges. *Biofabrication*, 12: 022001.

https://doi.org/10.1088/1758-5090/ab6034

37. Ge Q, Li Z, Wang Z, *et al.*, 2020, Projection micro stereolithography based 3D printing and its applications. *Int J Extrem Manuf*, 2: 022004.

https://doi.org/10.1088/2631-7990/ab8d9a.

38. Lee MP, Cooper G.J.T, Hinkley T, *et al.*, 2015, Development of a 3D printer using scanning projection stereolithography. *Sci Rep*, 5: 9875.

https://doi.org/10.1038/srep09875

39. Ahn D, Stevens LM, Zhou K, *et al.*, 2020, Rapid high-resolution visible light 3D printing. *ACS Cent Sci*, 6: 1555–1563.

https://doi.org/10.1021/acscentsci.0c00929

40. Sun C, Fang N, Wu DM, *et al.*, 2005, Projection micro-stereolithography using digital micro-mirror dynamic mask. *Sens Actuators A Phys*, 121: 113–120.

https://doi.org/10.1016/j.sna.2004.12.011

41. Behroodi E, Latifi H, Najafi F, 2019, A compact LED-based projection microstereolithography for producing 3D microstructures. *Sci Rep*, 9: 19692.

https://doi.org/10.1038/s41598-019-56044-3

42. Liu Y, Nolte DD, Pyrak-Nolte LJ, 2010, Large-format fabrication by two-photon polymerization in SU-8. *Appl Phys A*, 100: 181–191.

https://doi.org/10.1007/s00339-010-5735-8

43. Gong H, Bickham BP, Woolley AT, *et al.*, 2017, Custom 3D printer and resin for 18 μm × 20 μm microfluidic flow channels. *Lab Chip*, 17: 2899–2909.

https://doi.org/10.1039/C7LC00644F

44. Ricci D, Nava M, Zandrini T, *et al.*, 2017, Scaling-Up Techniques for the nanofabrication of cell culture substrates via two-photon polymerization for industrial-scale expansion of stem cells. *Materials* (*Basel*), 10: 66.

https://doi.org/10.3390/ma10010066

45. Trautmann A, Rüth M, Lemke HD, *et al.*, 2018, Two-photon polymerization based large scaffolds for adhesion and proliferation studies of human primary fibroblasts. *Opt Laser Technol*, 106: 474–480.

    https://doi.org/10.1016/j.optlastec.2018.05.008

46. Weisgrab G, Guillaume O, Guo Z, *et al.*, 2020, Ovsianikov, 3D printing of large-scale and highly porous biodegradable tissue engineering scaffolds from poly(trimethylene-carbonate) using two-photon-polymerization. *Biofabrication*, 12: 045036.

    https://doi.org/10.1088/1758-5090/abb539

47. Stender B, Hilbert F, Dupuis Y, *et al.*, 2019, Manufacturing strategies for scalable high-precision 3D printing of structures from the micro to the macro range. *Adv Opt Technol*, 8: 225–231.

    https://doi.org/10.1515/aot-2019-0022

48. Zhu W, Tringale KR, Woller SA, *et al.*, 2018, Rapid continuous 3D printing of customizable peripheral nerve guidance conduits. *Mater Today*, 21: 951–959.

    https://doi.org/10.1016/j.mattod.2018.04.001

49. Ren M, Lu W, Shao Q, *et al.*, 2021, Aberration-free large-area stitch-free 3D nano-printing based on binary holography. *Opt Express*, 29: 44250.

    https://doi.org/10.1364/OE.446503

50. What are Cylinder Lenses? Barrington: Edmund Optics, (n.d.), Available from: https://www.edmundoptics.com/knowledge-center/application-notes/optics/what-are-cylinder-lenses [Last accessed on 2022 Jul 13].

51. Goodman JW, 1996, Introduction to Fourier Optics. 2nd ed. New York: McGraw-Hill.

52. Jacobs PF, 1992, Rapid Prototyping and Manufacturing. 1st ed. Southfield: Society of Manufacturing Engineers.

53. Sigma-Aldrich.Com, 3-(Trimethoxysilyl)propyl methacrylate Product Information, (n.d.), 6514. Available from: https://www.sigmaaldrich.com/deepweb/assets/sigmaaldrich/product/documents/139/774/m6514pis.pdf [Last accessed on 2022 May 19].

54. Wang Z, Abdulla R, Parker B, et al., 2015, A simple and high-resolution stereolithography-based 3D bioprinting system using visible light crosslinkable bioinks. Biofabrication, 7: 045009.

    https://doi.org/10.1088/1758-5090/7/4/045009

55. Zhang R, Larsen NB, 2017, Stereolithographic hydrogel printing of 3D culture chips with biofunctionalized complex 3D perfusion networks. *Lab Chip*, 17: 4273–4282.

    https://doi.org/10.1039/c7lc00926g

56. Texas Instruments, (n.d.), DLP Getting Started. DLP Products. Dallas: TI.com. Available from: https://www.ti.com/dlp-chip/getting-started.html#choose_DLP [Last accessed on 2022 Mar 16].

57. Texas Instruments, (n.d.), UV Products (< 400 nm). Dallas: TI.com. Available from: https://www.ti.com/dlp-chip/3d-printing-direct-imaging/ultraviolet/overview.html [Last accessed on 2022 Jun 29].

58. Special Optics. Scanning Lens Theory. New Jersey: Special Optics. Available from: https://www.specialoptics.com/support/resources [Last accessed on 2022 Jul 13].

59. Bumstead JR, Park JJ, Rosen IA, *et al.*, 2018, Designing a large field-of-view two-photon microscope using optical invariant analysis. *Neurophotonics*, 5: 025001.

    https://doi.org/10.1117/1.nph.5.2.025001

60. Optics S, Production of Optical Components of Highest Quality-*f*-theta Lenses. Available from: https://www.silloptics.de/en/products/laser-optics/f-theta-lenses-1 [Last accessed on 2022 Jul 13].

61. Optics S, (n.d.), Stock F-Theta Lenses. Available from: https://www.shanghai-optics.com/stock-optics/stock-f-theta-lenses [Last accessed on 2022 Jul 13].

62. Mondschein RJ, Kanitkar A, Williams CB, *et al.*, 2017, Polymer structure-property requirements for stereolithographic 3D printing of soft tissue engineering scaffolds. *Biomaterials*, 140: 170–188.

    https://doi.org/10.1016/j.biomaterials.2017.06.005